Numerical determination of the sealing performance of a rough surface; real versus synthetic fractal surface

Christophe Vallet, Didier Lasseux, Philippe Sainsot, Hassan Zahouani

To cite this version:

Christophe Vallet, Didier Lasseux, Philippe Sainsot, Hassan Zahouani. Numerical determination of the sealing performance of a rough surface; real versus synthetic fractal surface. ASME 2008 Pressure Vessels and Piping Conference, Jul 2008, Chicago, United States. pp.1-10, 10.1115/PVP2008-61213 . hal-04540769

HAL Id: hal-04540769
https://hal.science/hal-04540769v1

Submitted on 10 Apr 2024

NUMERICAL DETERMINATION OF SEALING PERFORMANCE OF A ROUGH CONTACT: REAL VERSUS SYNTHETIC FRACTAL SURFACES

Christophe Vallet[*]
Didier Lasseux
TREFLE
CNRS UMR8508
Esplanade des Arts et Métiers
33405 Talence Cedex, France
Email: christophe.vallet@bordeaux.ensam.fr

Philippe Sainsot
LaMCoS, INSA-Lyon
CNRS UMR5259
F69621, France

Hassan Zahouani
ENISE
58 rue Jean Parot
42000 Saint Etienne, France

ABSTRACT

In this work, we adress the issue of sealing performance of metal gaskets using a deterministic approach that allows the analysis of creeping viscous flow and diffusion through a tight contact between rough surfaces taking into account surface deformation. Our analysis is focused on rough surfaces exhibiting fractal properties, and our purpose is to study the validity of the use of synthetic fractal surfaces as a representation of real ones.

Two kinds of real surfaces, obtained from two machining processes - lapping and sand-blasting - are considered. After checking the fractal nature of these surfaces, equivalent fractal ones are synthesized. Distributions of contact areas on the one hand, and transport properties K (for viscous flow) and D (for diffusion) on the other, obtained from real and synthetic surfaces are compared for a wide range of tightening. This comparison leads to the conclusion that the fractal representation is adequate to predict mechanical and transport properties of a contact between lapped or sand-blasted surfaces. Finally, using synthetic surfaces, it is shown that sealing performance of a rough contact decreases when the arithmetic roughness Ra and the fractal dimension D_f increase.

1 Introduction

In many industrial applications, as in the water primary circuit of nuclear power plants or in cryotechnologic rocket engines, for which thermodynamic conditions are severe, seal is performed by a direct contact between metallic surfaces [1]. Unfortunately, since no machining process can produce an ideally smooth surface, contact between two real surfaces is not perfect, and thus sealing is not complete. In this configuration, sealing efficiency, which is obtained by roughness flattening, mainly depends on surface textures. The determination of viscous flow and diffusion through a connected aperture field, i.e. all spaces left opened between surfaces, is also of major interest, since it allows the estimation of sealing performance of metal gaskets.

In this paper, we present a deterministic approach to estimate the transport properties of a rough contact, i.e. parameters relating the fluid flux to the driving force, from initial roughnesses while taking into account surface deflections. Here, this procedure is restricted to small scale defaults, which means that only microroughness is considered, eliminating form errors and waviness appearing at larger scales. Consequently, computations are performed on small surfaces, large enough, however, to be representative of microroughness. Thus, these surface elements are considered as the periodic unit cell of an infinite surface.

Our analysis is focused on rough surfaces, whose texture exhibits fractal properties. As reported by Majumdar and Bhushan [2], processes producing deterministic texture do not yield fractal surfaces, whereas those producing random texture do. Our purpose is to validate the use of synthetic fractal surfaces to predict the behavior of such a contact. This would avoid using real surfaces that require machining and detailed roughness measure-

---

[*] Address all correspondence to this author.

ment. The final goal is also to propose a predicting tool for leakage between such surfaces based on the fractal dimension and a roughness amplitude parameter only. To achieve this validation, a thorough comparison of contact areas as well as viscous and diffusive transport properties is performed between two real surfaces and their analogue synthesized ones. The two real surfaces under consideration are obtained by lapping and sand-blasting respectively.

In section 2, we determine fractal properties of real surfaces under consideration. Then, equivalent fractal surfaces are synthesized. In section 3, we first present an elasto-plastic deformation model which allows the determination of surface deflections caused by tightening. In a second step, we describe fluid flow models through a rough contact due to viscous and diffusive effects. The macroscopic viscous flow model introduces a transmissivity tensor **K** which linearly relates the viscous flow rate per unit width of the contact to the macroscopic pressure gradient in the fluid. Similarly, the macroscopic diffusive model introduces a diffusivity tensor **D** which linearly relates the diffusive flow rate per unit width of the contact to the macroscopic species gradient. We show that the two tensors **K** and **D** are intrinsic, i.e. they only depend on the aperture field h. Section 4 is dedicated to the comparison between real surfaces and their synthetic equivalent. This comparison is performed on the distributions of contact spots and on the transport properties of the rough contact. To illustrate the advantage of using synthetic surfaces, we investigate in section 5 the influence of roughness parameters (Ra and D_f) on the sealing performance of a rough contact, and more especially their influence on the transmissivity tensor **K**.

2 Analyses and simulation of isotropic fractal surfaces

A profile of a fractal surface is statistically self-affine, which means that a magnified part of this profile appears to be similar to the entire original one (Fig. 1). The power spectrum $P(\omega_x, \omega_y)$ of an isotropic fractal surface $z(x,y)$ follows a power law behavior given by [3]:

$$P(\omega_x, \omega_y) \propto |\tilde{z}(\omega_x, \omega_y)|^2 \propto \frac{1}{\omega_{eq}^{8-2D_f}} \qquad (1)$$

where $\tilde{z}(\omega_x, \omega_y)$ are the Fourier coefficients of $z(x,y)$, $\omega_{eq} = \sqrt{\omega_x^2 + \omega_y^2}$ and D_f is the fractal dimension. For a surface, $2 \leq D_f \leq 3$. It shall be noted that D_f, which can be estimated from the slope of $\log P = f(\log \omega_{eq})$, is related to the relative power of the frequency content and is an indicator of the degree of irregularity of the surface such that the larger D_f is, the more irregular the surface. For a whole characterization of rough surfaces, we need a second roughness parameter, which is related to the amplitude of all frequencies. In this work, we choose to consider the arithmetic roughness Ra, which is directly accessible from measurement and is widely used in engineering applications.

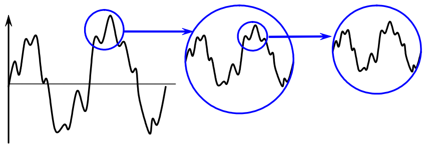

Figure 1. SELF-AFFINE PROFILE -

In this section, the fractal nature of a lapped surface and of a sand-blasted surface is investigated. The lapped surface was finished with abrasive particles of about 1 μm size while the sand-blasted surface was machined by streams of microbeads of $70-110$ μm size. The roughnesses of these surfaces were measured by white light interferometry on machined parts. Measurement parameters are given in Tab. 1. Surface dimensions L_x, L_y are assumed to be large enough and sampling intervals $\Delta_x = L_x/n_x$, $\Delta_y = L_y/n_y$ small enough to be representative of the microroughness. First, fractal properties of these textures are analyzed and then equivalent fractal surfaces are synthesized.

In Fig. 2(a), we have represented the power spectrum P of the real lapped surface versus the equivalent angular frequency ω_{eq}. Whereas some dispersion is observed, it appears that this surface exhibits fractal properties for ω_{eq} larger than a cut-off frequency $\omega_{\min}$, i.e. for wavelengths lower than $\frac{2\pi}{\omega_{\min}} = 20$ μm. For $\omega_{eq} < \omega_{\min}$, it will be assumed that P is constant (see [4]). The theoretical profile of P is fitted in the least squares sense, allowing the identification of D_f and $\omega_{\min}$. Similarly, the graph in Fig. 3(a) indicates that the real sand-blasted surface has a fractal trend for all frequencies investigated. These two surfaces have almost the same fractal dimension D_f (see Tab. 1), but since they have been machined with particles of different sizes, they are not fractal at the same scales. They also exhibit significant different roughness amplitudes as indicated by Ra values.

The approach to synthesize a fractal surface is based on the "Fourier filtering method" [3]. A random pattern a_{mn} ($1 \leq m \leq n_x$ and $1 \leq n \leq n_y$) is first generated in the physical space. A cor-

Table 1. SURFACE PARAMETERS -

Surface	L_x **x** L_y (μm)	n_x **x** n_y (points)	Ra (μm)	D_f
lapped	462 x 607	480 x 736	**0.4**	**2.50**
sand-blasted			**1.0**	**2.51**

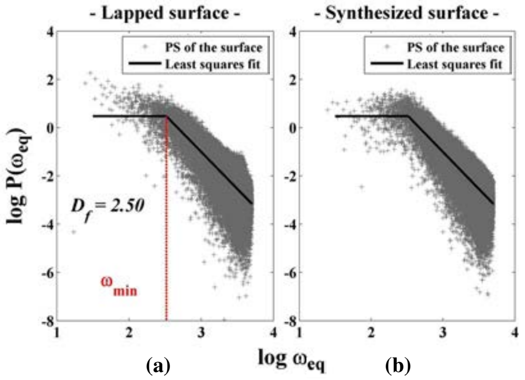

Figure 2. POWER SPECTRUM (PS) OF (a) A REAL LAPPED SURFACE AND (b) ITS EQUIVALENT SYNTHESIZED SURFACE -

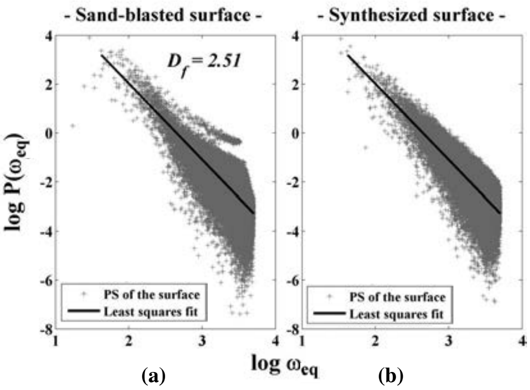

Figure 3. POWER SPECTRUM (PS) OF (a) A REAL SAND-BLASTED SURFACE AND (b) ITS EQUIVALENT SYNTHESIZED SURFACE -

relation among the Fourier coefficients $\tilde{a}_{kl}$ of a_{mn} is introduced such that moduli of $\tilde{z}_{kl}$ follow a power law as given by Eqn. (1):

$$\tilde{z}_{kl} = \frac{\tilde{a}_{kl}}{(\omega_{kl})^{4-D_f}} \tag{2}$$

where $\omega_{kl} = 2\pi\sqrt{\left(\frac{k}{L_x}\right)^2 + \left(\frac{l}{L_y}\right)^2}$.

The fractal surface z_{mn} is then obtained by a discrete inverse Fourier transform of $\tilde{z}_{kl}$:

$$z_{mn} = \frac{1}{n_x n_y}\sum_{k=0}^{n_x-1}\sum_{l=0}^{n_y-1}\tilde{z}_{kl}e^{\left(\mathrm{i}k\frac{2m\pi}{n_x}+\mathrm{i}l\frac{2n\pi}{n_y}\right)} \tag{3}$$

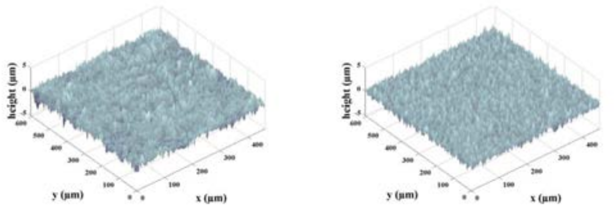

- Real lapped surface - - Synthesized lapped surface -

Figure 4. TEXTURES OF LAPPED SURFACES -

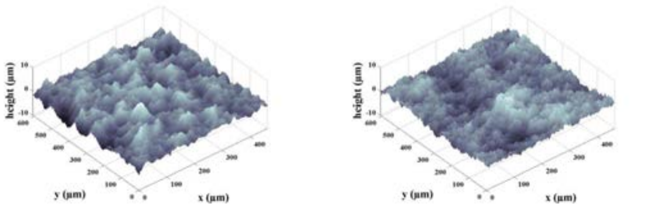

- Real sand-blasted surface - - Synthesized sand-blasted surface -

Figure 5. TEXTURES OF SAND-BLASTED SURFACES -

Finally, a rescaling is performed on z_{mn} to obtain the desired arithmetic roughness Ra:

$$\bar{z}_{mn} = \frac{Ra}{\frac{1}{n_x n_y}\sum\limits_{m=1}^{n_x}\sum\limits_{n=1}^{n_y}|z_{mn}|}z_{mn} \tag{4}$$

Equivalent fractal surfaces were synthesized with the roughness parameters of real surfaces (see Tab. 1). Power spectra of these synthesized surfaces are reported in Figs. 2(b) and 3(b). To synthesize the equivalent lapped surface, the cut-off angular frequency $\omega_{\min}$ was also considered in addition to the two parameters D_f and Ra. Textures of the real and synthesized lapped surfaces are represented in Fig. 4, while those of the sand-blasted surfaces are reported in Fig. 5. It appears that the textures of the lapped surfaces are more regular than those of the sand-blasted surfaces. This can be explained simply by the existence of the cut-off frequency $\omega_{\min}$ in the power spectrum of the lapped surface (see Fig. 2). This cut-off fades away long wavelength roughnesses leading to a texture smoother than those of the sand-blasted surfaces.

3 Deformation and transport models

3.1 Elasto-plastic deformation model

When two rough surfaces are brought in contact, effective contact only occurs on the top of asperities, which deform under the action of the applied load. During the past decades, the problem of the contact of rough surfaces has concentrated significant research efforts and a review of the main theories developed can be found in [5]. The major difficulty in modeling this problem comes from the description of the roughness, which can leads to a large number of data. The most widely used model is that proposed by Greenwood and Williamson [6], and then modified by many authors [7–9]. However, the adequacy of these models is questionable since assumptions made on asperities are most of the time unrealistic and since statistical roughness parameters used are not unique but strongly dependent on the resolution of the measuring instrument. With the expansion of computer capabilities, deterministic models have been developed. In that case, computations are directly performed on digitized surfaces, with no assumption on height distribution. In the present work, we adopted a simplified elasto-plastic deformation model. The problem is treated while supposing normal effects only, and to simplify, we consider the contact between a rough surface and a perfectly rigid and smooth plane. If the contact area is small compared to body dimensions and if slopes of asperities are small everywhere, solids in contact can be considered as semi-infinite. In that case, deflections of the rough surface are linked to the contact pressures by the relation [10, 11]:

$$u(\mathbf{x}) = \int\limits_S U(\mathbf{x},\xi)\, p^c(\xi)\, dS \tag{5}$$

Here, $u(\mathbf{x})$ is the surface deflection at point $\mathbf{x}(x,y)$ of the surface, $U(\mathbf{x},\xi)$ is the deflection at $\mathbf{x}$ due to a unit load at $\xi(\xi_x,\xi_y)$ while $p^c(\xi)$ designates the contact pressure at ξ and S the apparent contact surface.

When solids are elastic and homogeneous, the influence coefficient $U(\mathbf{x},\xi)$ can be expressed by the method of potentials proposed by Boussinesq [12]:

$$U(\mathbf{x},\xi) = \frac{1-\nu^2}{\pi E}\frac{1}{\sqrt{(x-\xi_x)^2+(y-\xi_y)^2}} \tag{6}$$

where E is the Young modulus and ν the Poisson ratio of the surface under consideration.

Contact pressures must also verify:

$$\frac{1}{S}\int\limits_S p^c(\mathbf{x})\, dS = \mathrm{Pca} \tag{7}$$

where Pca is the average applied contact pressure.

From Eqn. (5), we can notice that only the rough surface has to be discretized. Computational time is therefore drastically reduced in comparison with classical methods like finite element methods, which require the discretization of the entire volume.

If the rough surface is discretized by (n_x,n_y) identical cells of dimensions (Δ_x,Δ_y), the solution of the elastic deformation problem consist in solving the following system:

$$u_{ij} = \sum_{k=0}^{n_x-1}\sum_{l=0}^{n_y-1} U_{i-k,j-l}\, p^c_{kl}, \quad (0 \le i \le n_x, 0 \le j \le n_y) \tag{8a}$$

$$\frac{1}{n_x n_y}\sum_{k=0}^{n_x-1}\sum_{l=0}^{n_y-1} p^c_{ij} = \mathrm{Pca} \tag{8b}$$

$$u_{ij} = \delta_0 - h_{ij}, \quad (i,j) \in \Omega_c \tag{8c}$$

$$p^c_{ij} > 0, \quad (i,j) \in \Omega_c \tag{8d}$$

$$u_{ij} \ge \delta_0 - h_{ij}, \quad (i,j) \notin \Omega_c \tag{8e}$$

$$p^c_{ij} = 0, \quad (i,j) \notin \Omega_c \tag{8f}$$

where u_{ij} is the surface deflection at node (i,j), p^c_{ij} is the uniform contact pressure acting on the cell centered at node (i,j), $U_{i-k,j-l}$ are the influence coefficients, Ω_c is the set of grid nodes that are in contact, δ_0 is the rigid body displacement of the two solids and h_{ij} is the aperture at node (i,j) between undeformed surfaces.

To take into account plastic deformation, a plastic criterion is directly applied on contact pressures. Materials are assumed to follow an elastic-perfectly plastic behavior, i.e. contact pressures are bounded by the hardness $\mathcal{H}$ of the softer material. This simplified model does not take into account work-hardening that might significantly modify the deformation of asperities. However, this discussion on the choice of an adequate mechanical behavior is beyond the scope of this paper and the elastic-perfectly plastic model was selected to keep the approach simple and illustrative.

3.2 Fluid transport models

3.2.1 Micro-scale viscous flow and diffusion

In this section, we consider incompressible, isothermal and stationary mass transfer due to creeping viscous flow on the one hand and to diffusion on the other. Whereas diffusion through metal gaskets is negligible compared to viscous flow, we will see latter that the analysis of diffusive effects represents an additional independent test on the relevance of the fractal representation for the class of surfaces under consideration. At the micro-scale, viscous creeping flow (at negligible Reynolds number) through a rough fracture can be described by the Stokes model:

$$-\nabla p+\mu\nabla^2\mathbf{v}=0 \tag{9a}$$

$$\nabla.\mathbf{v}=0 \tag{9b}$$

$$\mathbf{v}.\mathbf{n}=0,\ \text{ at the solid wall} \tag{9c}$$

$\mathbf{v}$ being the fluid velocity, p the fluid pressure and μ its dynamic viscosity. In the same way, diffusion is described by Fick's law:

$$\nabla.\left(\mathcal{D}\nabla c\right)=0 \tag{10a}$$

$$\nabla c.\mathbf{n}=0\ \text{ at the solid wall} \tag{10b}$$

where $\mathcal{D}\nabla c$ is the diffusive flux, c the species concentration which diffuses through the contact and $\mathcal{D}$ the molecular diffusion coefficient.

If we assume that the aperture field $h\left(x,y\right)$ is slowly varying, i.e. that slopes of asperities are small, the two previous models can be reduced from 3D to 2D. This can be performed using an order of magnitude analysis and an integration of the balance equations in the direction normal to the mean plane of the contact (z-direction). Under these circonstances, viscous flow is described by the Reynolds model:

$$\mathbf{q}_v=-\frac{h^3}{12\mu}\nabla p\ \text{ in } \beta \tag{11a}$$

$$\nabla.\mathbf{q}_v=0\ \text{ in } \beta \tag{11b}$$

$$\mathbf{q}_v.\mathbf{n}=0\ \text{ on } C_{\beta\sigma} \tag{11c}$$

where β designates the fluid phase and σ the effective contact areas of contours $C_{\beta\sigma}$ in the x-y plane (see fig. 6); $\mathbf{q}_v=\int_0^h \mathbf{v}dz$ is the volume flow rate of the β-phase per unit width.

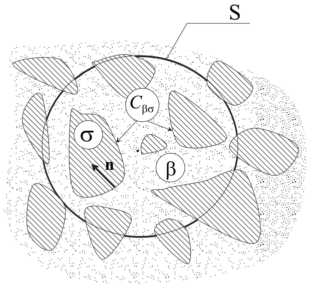

Figure 6. LOCAL CONTACT CONFIGURATION: CONTACT AREAS σ AND FLUID PHASE β -

In the same way, the diffusion problem becomes:

$$\mathbf{q}_d=-\mathcal{D}h\nabla c\ \text{ in } \beta \tag{12a}$$

$$\nabla.\mathbf{q}_d=0\ \text{ in } \beta \tag{12b}$$

$$\mathbf{q}_d.\mathbf{n}=0\ \text{ on } C_{\beta\sigma} \tag{12c}$$

$\mathbf{q}_d=\int_0^h \mathbf{j}dz$ is the molecular flow rate of the β-phase per unit width.

3.2.2 Transport properties of the rough contact

Equations (11) and (12) are formally identical. They can be rewritten in a generic form:

$$\mathbf{q}=-k\nabla\omega\ \text{ in } \beta \tag{13a}$$

$$\nabla.\mathbf{q}=0\ \text{ in } \beta \tag{13b}$$

$$\mathbf{q}.\mathbf{n}=0\ \text{ on } C_{\beta\sigma} \tag{13c}$$

with $k=\frac{h^3}{12\mu}$ and $\omega=p$ for viscous flow and $k=\mathcal{D}h$ and $\omega=c$ for diffusion.

By averaging these equations over a small portion S of the contact, the previous model can be up-scaled from micro to macro-scale. This operation allows to derive macroscopic models of transport relating the macroscopic flow rate at the scale of

S, to the macroscopic driving force (i.e. the macroscopic pressure gradient or species gradient). Moreover, it provides an explicit way to determine the transport coefficients appearing in these macroscopic models. The averaging process is similar to volume averaging [13] and is based on the definitions of the two operators applied on any quantity φ defined in the β -phase:

$$\langle \varphi \rangle = \frac{1}{S} \int\limits_{S_\beta} \varphi dS = \frac{1}{S_\beta + S_c} \int\limits_{S_\beta} \varphi dS \tag{14a}$$

and

$$\langle \varphi \rangle^\beta = \frac{1}{S_\beta} \int\limits_{S_\beta} \varphi dS \tag{14b}$$

along with the averaging theorem:

$$\langle \nabla \varphi \rangle = \nabla \langle \varphi \rangle + \frac{1}{S} \int\limits_{C_{\beta\sigma}} \mathbf{n} \varphi dS \tag{14c}$$

Using a procedure employed for similar problems [14]- [15], it can be shown that the generic macroscopic model takes the form:

$$\langle \mathbf{q} \rangle = -\mathbf{H} . \nabla \langle \omega \rangle^\beta \tag{15a}$$

$$\nabla . \langle \mathbf{q} \rangle = 0 \tag{15b}$$

In equation (15a), the tensor $\mathbf{H}$ can be explicitely determined from the aperture field according to:

$$\mathbf{H} = \langle k \left(\mathbf{I} + \nabla \mathbf{b} \right) \rangle \tag{16}$$

where $\mathbf{b}$ is solution of the closure problem that is written as:

$$\nabla . \left(k \nabla \mathbf{b} \right) = -\nabla \widetilde{k} \ \text{ in } \beta \tag{17a}$$

$$-\mathbf{n}_{\beta\sigma} . \nabla \mathbf{b} = \mathbf{n}_{\beta\sigma} \ \text{ on } C_{\beta\sigma} \tag{17b}$$

$$\mathbf{b} \left(\mathbf{x} + \mathbf{r}_i \right) = \mathbf{b} \left(\mathbf{x} \right) \tag{17c}$$

$$\langle \mathbf{b} \rangle = 0 \tag{17d}$$

In the above equations, $\widetilde{k} = k - \langle k \rangle$ and $\mathbf{r}_i$ is the surface element dimension in the i^{th} direction. This surface element is supposed to be representative of a periodic infinite structure. Note that $\mathbf{K}$ and $\mathbf{D}$ are intrinsic, i.e. only depends on h.

For viscous flow, the flow rate per unit width of the contact, at the scale of the surface element, is hence:

$$\langle \mathbf{q}_v \rangle = -\frac{\mathbf{K}}{\mu} . \nabla \langle p \rangle^\beta \tag{18a}$$

$$\nabla . \langle \mathbf{q}_v \rangle = 0 \tag{18b}$$

where $\mathbf{K} = \mathbf{H}$ is the intrinsic transmissivity tensor with $k = \frac{h^3}{12}$ (16) and (17). It must be noted that $\mathbf{K}$ has the dimension of cubic length.

In the same way, the flow rate per contact unit width resulting from diffusion at the scale of the surface element is given by:

$$\langle \mathbf{q}_d \rangle = -\mathcal{D} \mathbf{D} . \nabla \langle c \rangle^\beta \tag{19a}$$

$$\nabla . \langle \mathbf{q}_d \rangle = 0 \tag{19b}$$

where $\mathbf{D} = \mathbf{H}$ is the effective diffusivity tensor with $k = h$ in (16) and (17). Note that $\mathbf{D}$ has the dimension of length.

From Eqns. 18a and 19a, viscous and diffusive flow rates through the contact can be fully characterized from $\mathbf{K}$ and $\mathbf{D}$ only, that is why, in the following, we consider transport properties and not flow rates. Moreover, it can be noted that $\mathbf{D}$ involves an average over h while $\mathbf{K}$ involves an average over h^3. Hence, although diffusion through metal gaskets is negligible compared to viscous effects, the combined study of $\mathbf{K}$ and $\mathbf{D}$ provides two discriminating tests to validate the use of synthetic surfaces instead of real surfaces.

Equations (17) were derived while considering a continuous aperture field. However, if roughness is measured on a set of n_x x n_y points so that the surface is represented by n_x x n_y cells, each of them having a constant aperture h_i, the discrete form of the closure problem (17) is:

$$i^{th} \text{ cell: } \nabla . \nabla \mathbf{b}_i = 0 \tag{20a}$$

$$ij \text{ interface: } \mathbf{n} . k_i \left(\nabla \mathbf{b}_i + \mathbf{I} \right) = \mathbf{n} . k_j \left(\nabla \mathbf{b}_j + \mathbf{I} \right) \tag{20b}$$

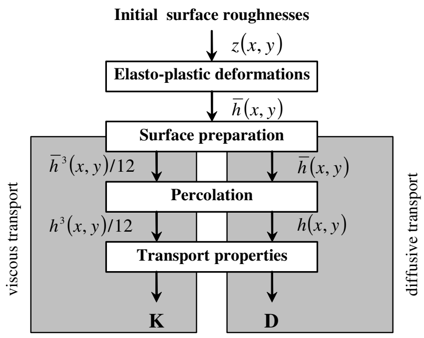

Figure 7. COMPUTATIONAL ALGORITHM FLOWCHART -

$$ij \text{ interface: } \mathbf{b}_i = \mathbf{b}_j \tag{20c}$$

$$j^{th} \text{ cell: } \nabla.\nabla\mathbf{b}_j = 0 \tag{20d}$$

$$\sum_i b_i = 0 \tag{20e}$$

Equations (20b) and (20c) allow the continuity of $\mathbf{n}.\mathbf{q}$ and ω respectively, between each cell. Moreover, at the scale of the surface element, $\mathbf{b}$ is assumed to be periodic.

3.3 Algorithm

The computational algorithm used to determine transport properties of a rough contact is schematized in Fig. 7. It is initiated with a set of n_x x n_y points $z(x,y)$ describing a representative surface element either of the real or synthesized surface. The aperture field $h(x,y)$ resulting from deformation of the initial surface $z(x,y)$ is computed with the elasto-plastic deformation model as described above. Intrinsic transmissivity and diffusivity tensors, **K** and **D** respectively, are computed using the same numerical procedure. Distinction between viscous and diffusive effects is performed by the surface preparation module. The percolation module allows to remove all non percolating clusters, i.e. non contact areas not connected to surface edges.

4 Real versus synthetic surface

In this section, we consider the contact between one of the rough surfaces presented in section 2 and a perfectly rigid and smooth plane. Results obtained from real and synthesized surfaces are compared in order to validate the use of synthetic fractal surfaces for lapping and sand-blasting processes. Two aspects are investigated: the distribution of contact spots on the one hand and viscous and diffusive transport properties of the contact on the other. Computations were performed for several average contact pressures Pca ranging from 7 to 600 MPa and considering the mechanical properties of stainless steel, i.e. $E = 210\ GPa$, $\nu = 0.3$ and $\mathcal{H} = 1800\ MPa$. Although machining might modify mechanical properties (namely hardness) on the surface, we kept the bulk-material value for $\mathcal{H}$ in absence of thorough validated results on this mechanism.

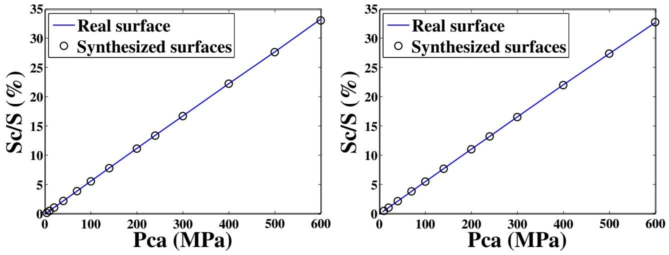

- Lapped surface - - Sand-blasted surface -

Figure 8. RELATIVE CONTACT AREA S_c/S VERSUS AVERAGE CONTACT PRESSURE Pca -

Several fractal surfaces were synthesized using the same roughness parameters but changing the initial random sequence a_{mn}. Thus, for each kind of texture (lapped and sand-blasted), four different surfaces were synthesized from the power spectra of the real surfaces considered in section 2.

4.1 Effective contact areas

In Fig. 8, we have represented the ratio of the true contact area S_c to the nominal surface area $S = L_x L_y$ versus the average contact pressure Pca. The linear dependence of S_c/S on Pca is confirmed and an excellent agreement is observed between real and synthesized surfaces. However, it must be noticed that the successful comparison between the effective contact areas is not sufficiently discriminating since lapped and sand-blasted surfaces exhibit identical variations of S_c/S versus Pca, although these surfaces have roughness parameters that are significantly different. As a consequence, a more detailed study on the distribution of contact areas is necessary.

In Figs. 9 and 10, we have reported the mean, m, and the standard deviation, σ, of the distribution of contact spot areas versus the contact pressure Pca for lapped and sand-blasted surfaces respectively. For lapped surfaces, we can observe that all the synthesized surfaces have a similar behavior, while for sand-blasted surfaces, a more significant dispersion between the four realizations is observed. As noticed in section 2, lapped surfaces differ from sand-blasted ones in the relative power of low frequencies. Contrary to lapped surfaces, the dominant pattern of sand-blasted surfaces is determined by the longer wavelengths close to the scale of the surface element under consideration.

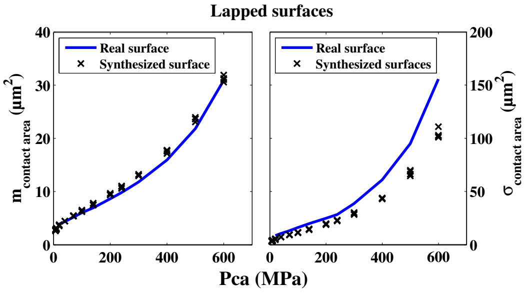

Figure 9. MEAN, m, AND STANDARD DEVIATION, σ, OF THE DISTRIBUTION OF CONTACT SPOT AREAS OF LAPPED SURFACES -

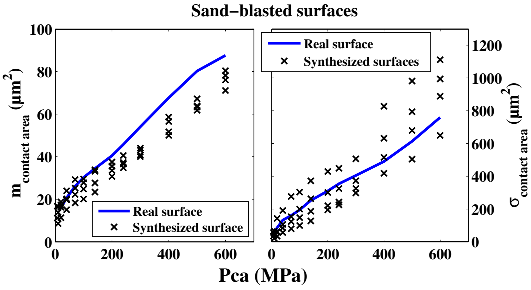

Figure 10. MEAN, m, AND STANDARD DEVIATION, σ, OF THE DISTRIBUTION OF CONTACT SPOT AREAS OF SAND-BLASTED SURFACES -

Thus, while changing the initial random sequence a_{mn}, the texture of sand-blasted surfaces is more affected than that of lapped surfaces, that is why a significant scatter is observed among synthesized sand-blasted surfaces and not among synthesized lapped surfaces.

As can be seen in Fig. 9, a good agreement between real and synthesized lapped surfaces is observed on the mean, m, of the contact spot areas since relative deviations between real and synthesized surfaces are smaller than 10%. The comparison of the standard deviations σ shows that this parameter is more sensitive since relative deviations are about 30%.
Deviations between the mean of the real sand-blasted surface and the average value of the corresponding synthesized surfaces (Fig. 10) can reach 20%, which remains fully consistent in comparison to the relative dispersion on the four realizations of synthesized surfaces (about 15%). Results concerning the standard deviation σ show a good agreement between real and synthesized surfaces since results obtained on the real surface fall well within the range of those obtained on synthesized surfaces.

4.2 Effective transport properties

Because of machining process, surfaces under investigation here are expected to be isotropic in the x-y plane, featuring spherical **K** and **D** tensors, i.e. **K** =K**I** and **D** =D**I**. Our numerical results confirm this property (at least for lapped surface; see discussions below). In fact, off-diagonal terms for the two types of surfaces were, at least, two orders of magnitude smaller than diagonal terms. As a consequence, our discussion is focused on the diagonal terms of **K** and **D**. Figure 11 shows the log-log plots of these diagonal terms for the real and synthesized lapped surfaces versus Pca. This figure clearly indicates that the real surface is perfectly isotropic at the scale of investigation. All synthesized surfaces have the same transport properties, except at high contact pressure Pca where some dispersion can be observed. At low Pca, the number of branches of the percolating cluster, i.e. paths where the fluid can flow, is large, explaining why all surfaces are statistically identical. When increasing Pca, the number of branches decreases, leading to scattered values of K and D. Moreover, transport properties rapidly decrease with the increasing of the contact pressure which confirms that tightening makes the contact less percolating. Whereas experimental results obtained on turned surfaces indicate that both K and D depend on Pca according to a power law [16], effective transport properties of fractal surfaces exhibit a more complex behavior. It must be noticed that the range of variation of K is much wider than that of D, and this is due to the fact that this later quantity is related to the aperture field h while the former is related to h^3. For both K and D, an excellent agreement is obtained between real and synthesized surfaces. Whatever Pca, relative deviations remain smaller than 7% on the estimation of D. It can reach 20% on the estimation of K, which is small compared to the range of variation of K over roughly three orders of magnitude for the range of Pca under consideration.

In Fig. 12, we have reported the diagonal terms of **K** and **D** estimated on the real and synthesized sand-blasted surfaces. In contrast to lapped surfaces, diagonal terms are significantly different as evidenced by results on the real surface. The same behavior is observed on each of the four realizations. For each surface, at a given value of Pca, relative deviations of diagonal terms with respect to their average value increase with contact pressure Pca. As for lapped surfaces, this is due to the number of branches of the percolating cluster which decreases when Pca increases. These deviations can reach 20% for diffusivity and 45% for transmissivity. Anisotropy of the transport properties is a result of a size effect, as already discussed above for the distribution of contact spot areas. Since the fractal character of this surface remains at a scale equal to the size L_x, L_y of the surface element under investigation, dispersion is expected on its behavior that must be analyzed on average over several realizations. However, as for lapped surfaces, a very good agreement between computed transport properties is obtained between real and synthesized sand-blasted surfaces. Along with results on effective

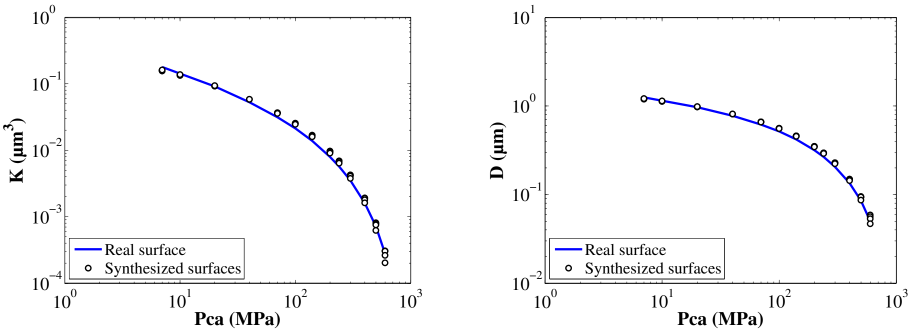

- Transmissivity - **- Diffusivity -**

Figure 11. TRANSPORT PROPERTIES OF REAL AND SYNTHESIZED LAPPED SURFACES -

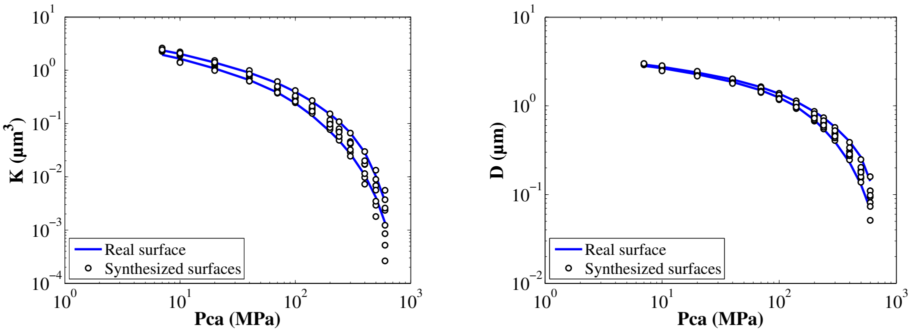

- Transmissivity - **- Diffusivity -**

Figure 12. TRANSPORT PROPERTIES OF REAL AND SYNTHESIZED SAND-BLASTED SURFACES -

contact areas, this validates the use of synthesized surfaces for the estimation of both the effective contact and transport properties of a rough contact between fractal surfaces. This provides a useful tool to analyze the influence of roughness parameters on transport properties as shortly proposed bellow.

5 Influence of Ra and D_f on $\mathbf{K}$

In this section, the influence of Ra and D_f on the transmissivity $\mathbf{K}$ is illustrated. The effect of Ra is studied by synthesizing five surfaces with $D_f = 2.5$ and Ra varying from 0.1 μm to 2 μm. The effect of D_f is studied by synthesizing four surfaces with $Ra = 1$ μm and D_f varying from 2.1 to 2.7, which is in accordance with measurements performed on real surfaces [17, 18]. For all surfaces, $L_{x,y} = 1$ mm, $n_{x,y} = 256$ and $\omega_c = 0$. Moreover, computations were performed for Pca $\in \{40;\ 100;\ 200;\ 300;\ 400;\ 500\}$ MPa.

Figure 13 shows variations of K versus Ra on the one hand and versus D_f on the other for each Pca under consideration. Whatever Pca, Ra has the same effect. As expected, K increases with Ra, which means that sealing performance of the rough contact decreases when contacting surfaces have large Ra. Although always increasing with D_f, $\mathbf{K}$ is shown to be more sensitive to this parameter at large values of Pca. At small values of Pca, the dependency of $\mathbf{K}$ on D_f obeys roughly a power law. As explained in section 2, fractal surfaces become more irregular when D_f increases, leading to a smaller contact area and hence decreasing sealing performance. However, in the range of Ra and D_f investigated, the effect of D_f is much less significant than that of Ra.

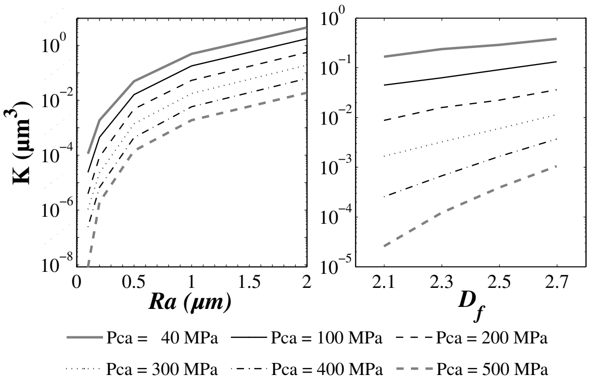

Figure 13. ROUGHNESS PARAMETERS EFFECT ON K -

6 Conclusions

A global and deterministic approach for determining sealing performance of metal gasket from surface textures, taking into account roughness deformation, has been presented. The study was carried out on a class of rough surfaces exhibiting fractal properties. The fractal nature of lapped and sand-blasted surfaces was confirmed from direct measurements.

Equivalent fractal surfaces were synthesized with the same fractal properties as the real ones and a thorough comparison of contact areas on the one hand and of transport properties on the other, was performed between real and synthesized surfaces. Due to the existence of the cut-off frequency, the study on lapped surfaces shows that when synthesizing several surfaces with the same roughness parameters, results are almost identical. This is not true for sand-blasted surfaces and significant dispersions are observed between results obtained from four realizations of synthesized surfaces. For the same reasons, at the scale of the surfaces investigated in this work, transport properties of lapped surfaces are isotropic whereas due to a size effect, transport properties of sand-blasted surfaces are anisotropic.

The main result of this work is twofold. First, distributions of contact areas of the synthesized surfaces were shown to be in good agreement with those of the real surfaces. Secondly, a very good agreement was obtained between real and synthesized surfaces during the estimation of viscous and diffusive transport properties, for both lapped and sand-blasted surfaces. This represents a set of very discriminating comparisons leading to the conclusion that synthesized surfaces can be used to describe contact mechanics and contact transport properties through a contact between rough surfaces produced by a random machining process.

Finally, using synthetic surfaces, it was shown that sealing performance of a rough contact decreases when Ra and D_f increases, and that the effect of Ra is more significant than that of D_f.

ACKNOWLEDGMENT

Financial support from EDF R&D as well as from CNES, SNECMA and CNRS are gratefully acknowledged.

REFERENCES

[1] Marie, C., Lasseux, D., Zahouani, H., and Sainsot, P., 2003. "An integrated approach to characterize liquid leakage through metal contact seal". *European Journal Mech. and Env. Eng.,* **48**(2), pp. 81–86.

[2] Majumdar, A., and Bhushan, B., 1990. "Role of fractal geometry in roughness characterization and contact mechanics of surfaces". *Journal of Tribology,* **112**, pp. 205–216.

[3] Peitgen, H., and Saupe, D., 1988. *The Science of Fractal Images*. Springer-Verlag, New York.

[4] Persson, B., Albohr, O., Tartaglino, U., Volokitin, A., and Tosatti, E., 2005. "On the nature of surface roughness with application to contact mechanics, sealing, rubber friction and adhesion". *J. Phys.: Condens. Matter,* **17**, pp. R1–R62.

[5] Bhushan, B., 1998. "Contact mechanics of rough surfaces in tribology: Multiple asperity contact". *Tribology Letters 4*, pp. 1–35.

[6] Greenwood, J., and Williamson, J., 1966. "Contact of nominally flat surfaces". *Proc. Roy. Soc. London,* **A295**, pp. 300–319.

[7] Chang, W., Etsion, I., and Bogy, D., 1987. "An elastic-plastic model for the contact of rough surfaces". *Journal of Tribology,* **109**, pp. 257–263.

[8] Nayak, P., 1973. "Random process model of rough surfaces in plastic contact". *Wear,* **26**, pp. 305–333.

[9] Bush, A., Gibson, R., and Keogh, G., 1979. "Strongly anisotropic rough surfaces". *Journal of Lubrication Technology,* **101**, pp. 15–20.

[10] Mayeur, C., Sainsot, P., and Flamand, L., 1995. "A numerical elastoplastic model for rough contact". *Journal of Tribology,* **117**, pp. 422–429.

[11] Sainsot, P., Jacq, C., and Nélias, D., 2002. "A numerical model for elastoplastic rough contact". *CMES,* **3**(4), pp. 497–506.

[12] Johnson, K., 1985. *Contact Mechanics*. Cambridge University Press, Cambridge.

[13] Whitaker, S., 1999. *The Method of Volume Averaging, Theory and Application of Transport in Porous Media*. Kluwer Academic Publishers.

[14] Prat, M., Plouraboué, F., and Letalleur, N., 2002. "Averaged Reynolds equation for flow between rough surfaces in sliding motion". *Transport in Porous Media,* **48**, pp. 291–313.

[15] Quintard, M., and Whitaker, S., 1987. "Ecoulement monophasique en milieux poreux : Effets des hétérogénéités locales". *Journal de Mécanique Théorique et Appliquée,* **6**, pp. 691–726.

[16] Marie, C., and Lasseux, D., 2007. "Experimental leak-rate measurement through a static metal seal". *Journal of Fluids Engineering,* **129**(6), pp. 799–805.

[17] Majumdar, A., and Tien, C., 1990. "Fractal characterization and simulation of rough surfaces". *Wear,* **136**, pp. 313–327.

[18] Ganti, S., and Bhushan, B., 1995. "Generalized fractal analysis and its applications to engineering surfaces". *Wear,* **180**, pp. 17–34.